ADVANCED MATERIALS
www.advmat.de

Co-Self-Assembled Monolayers Modified NiO_x for Stable Inverted Perovskite Solar Cells

Qi Cao, Tianyue Wang, Xingyu Pu, Xilai He, Mingchao Xiao, Hui Chen, Lvchao Zhuang, Qi Wei, Hok-Leung Loi, Peng Guo, Bochun Kang, Guangpeng Feng, Jing Zhuang, Guitao Feng, Xuanhua Li, and Feng Yan**

[4-(3,6-dimethyl-9H-carbazol-9yl)butyl]phosphonic acid (Me-4PACz) self-assembled molecules (SAM) are an effective method to solve the problem of the buried interface of NiO_x in inverted perovskite solar cells (PSCs). However, the Me-4PACz end group (carbazole core) cannot forcefully passivate defects at the bottom of the perovskite film. Here, a Co-SAM strategy is employed to modify the buried interface of PSCs. Me-4PACz is doped with phosphorylcholine chloride (PC) to form a Co-SAM to improve the monolayer coverage and reduce leakage current. The phosphate group and chloride ions (Cl^-) in PC can inhibit NiO_x surface defects. Meantime, the quaternary ammonium ions and Cl^- in PC can fill organic cations and halogen vacancies in the perovskite film to enable defects passivation. Moreover, Co-SAM can promote the growth of perovskite crystals, collaboratively solve the problem of buried defects, suppress nonradiative recombination, accelerate carrier transmission, and relieve the residual stress of the perovskite film. Consequently, the Co-SAM modified devices show power conversion efficiencies as high as 25.09% as well as excellent device stability with 93% initial efficiency after 1000 h of operation under one-sun illumination. This work demonstrates the novel approach for enhancing the performance and stability of PSCs by modifying Co-SAM on NiO_x.

1. Introduction

NiO_x, an inorganic p-type semiconductor, is commonly utilized as the hole transport layer (HTL) in inverted and tandem perovskite solar cells (PSCs) due to its cost-effectiveness, stability, and scalability.[1] Notably, the NiO_x-inverted PSC has recently achieved a certified power conversion efficiency (PCE) of 25.58%.[2] However, there is still room for improvement as the highest authenticated PCE stands at 26.14%. The presence of oxygen vacancies and uncoordinated metal ion defects on the NiO_x surface contributes to this potential for enhancement.[3] Additionally, submicron-scale defects exist on the lower surface of the perovskite material.[4] The interaction between NiO_x and the perovskite film also leads to interface reactions, resulting in nonradiative recombination at the interface.[5] These phenomena adversely affect device stability and cause a loss of open-circuit voltage (V_{OC}), which poses a significant obstacle to achieving high-efficiency and highly stable inverted PSCs. Therefore, addressing these issues is crucial for advancing the performance of inverted PSCs.

To address the interface problem in NiO_x/perovskite heterojunctions, various strategies have been employed, such as the use of inorganic salts,[6] self-assembled monolayers (SAMs),[7] organic molecules,[8] and 2D materials,[9] to modify and passivate the buried interface. Li et al. successfully improved the interface by utilizing SAM-processed NiO_x nanocrystals, which effectively bridged the perovskite film. This approach created a hole-selective contact that mitigated interface recombination and facilitated hole extraction. As a result, they achieved a remarkable efficiency of 24.7% (certified as 24.4%) in a flexible all-perovskite tandem solar cell.[10] In a similar vein, Huang et al. employed

---

Q. Cao, T. Wang, M. Xiao, L. Zhuang, Q. Wei, H.-L. Loi, B. Kang,
J. Zhuang, G. Feng, F. Yan
Department of Applied Physics
The Hong Kong Polytechnic University
Hung Hom, Kowloon, Hong Kong SAR 999077, P. R. China
E-mail: apafyan@polyu.edu.hk

The ORCID identification number(s) for the author(s) of this article can be found under https://doi.org/10.1002/adma.202311970

© 2024 The Author(s). Advanced Materials published by Wiley-VCH GmbH. This is an open access article under the terms of the Creative Commons Attribution License, which permits use, distribution and reproduction in any medium, provided the original work is properly cited.

DOI: 10.1002/adma.202311970

Q. Cao, X. Pu, X. He, H. Chen, P. Guo, G. Feng, X. Li
State Key Laboratory of Solidification Processing
Center for Nano Energy Materials
School of Materials Science and Engineering
Northwestern Polytechnical University
Xi'an 710072, P. R. China
E-mail: lixh32@nwpu.edu.cn

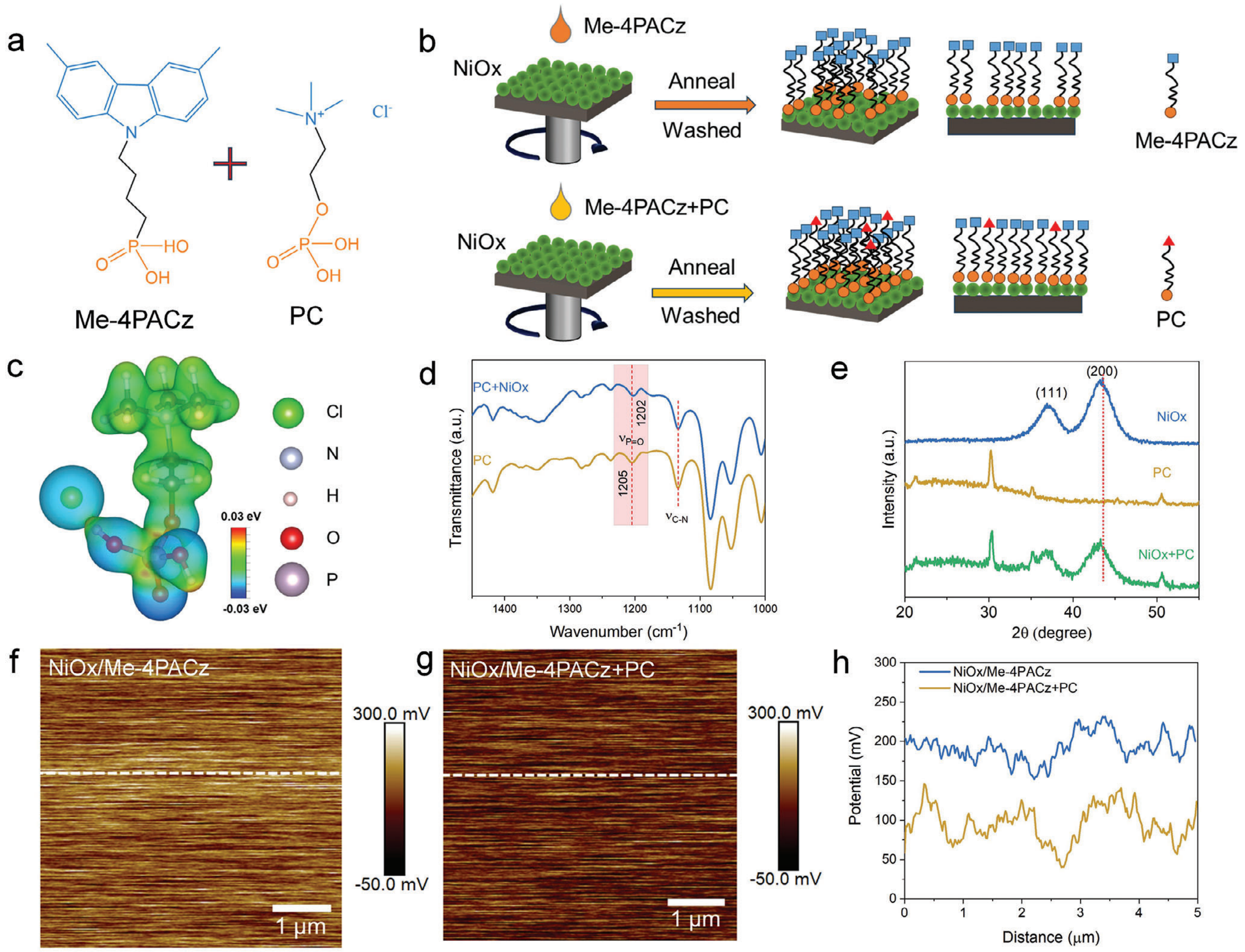

Figure 1. Effect of Co-SAM on NiO_x properties. a) Molecular structures of Me-4PACz and PC. b) Schematic illustration of SAM (Me-4PACz) and Co-SAM (Me-4PACz+PC) of modified NiO_x. c) Gaussian calculated electrostatic potential of PC molecule. d) FTIR of PC+NiO_x and PC. e) XRD of NiO_x, PC, and PC+ NiO_x. KPFM images of f) NiO_x/Me-4PACz and g) NiO_x/Me-4PACz+PC. h) CPD changes of NiO_x/Me-4PACz and NiO_x/Me-4PACz+PC films.

[4-(3,6-dimethyl-9H-carbazol-9yl)butyl]phosphonic acid (Me-4PACz) to address interface defects in the NiO_x/formamidinium lead triiodide ($FAPbI_3$) junction. By reducing these defects and improving carrier transport, they achieved an PCE of 23.56% in an inverted $FAPbI_3$ based PSCs.[11] Researchers have continued to refine the design of SAMs, leading to significant advancements in the development of high-performance photovoltaic devices.[12,13] SAMs composed of carbazole core and phosphonic acid, such as 2PACz ([2-(9H-Carbazol-9-yl)ethyl]phosphonic acid) and Me-4PACz, are particularly prevalent due to their maturity in industrial applications.[14,15] However, despite the widespread use of these SAMs, there are certain limitations that need to be addressed. The steric hindrance of the carbazole core restricts the formation of a dense single molecule layer on the substrate, hampering effective passivation of bottom defects in the perovskite film. Consequently, this can lead to issues such as leakage current and nonradiative recombination, adversely affecting the performance and stability of optoelectronic devices.

Here, we modify the buried interface of NiO_x-based PSCs by doping Me-4PACz with phosphorylcholine chloride (PC) to form Co-SAM (**Figure 1**a) for improving the monolayer coverage. The phosphate group and chloride ions (Cl^-) in PC can inhibit NiO_x surface defects. Meantime, the quaternary ammonium ions and Cl^- in PC can fill organic cations and halogen vacancies defects at the bottom of the perovskite film. Co-SAM can promote the growth of perovskite crystals, collaboratively solve the problem of buried defects, suppress nonradiative recombination, accelerate carrier transmission, and relieve the residual stress of the perovskite film. Therefore, the maximum efficiency of the Co-SAM modified device reaches 25.09%. And the operational stability of the device is improved, maintaining 93% of the initial efficiency after continuous running for 1000 h under one-sun illumination.

2. Results and Discussion

To highlight the advantages of Co-SAM, we drew a schematic diagram in Figure 1b. Spin-coating of SAM alone on NiO_x cannot

© 2024 The Author(s). Advanced Materials published by Wiley-VCH GmbH

15214095, 2024, 16, Downloaded from https://onlinelibrary.wiley.com/doi/10.1002/adma.202311970 by Hong Kong Poly University, Wiley Online Library on [23/06/2024]. See the Terms and Conditions (https://onlinelibrary.wiley.com/terms-and-conditions) on Wiley Online Library for rules of use; OA articles are governed by the applicable Creative Commons License

form a dense monolayer due to the steric hindrance effect, while Co-SAM easily forms a dense and uniform single monolayer because PC can fill the vacancies within the SAM structure, ensuring more complete coverage. The phosphate groups, quaternary ammonium ions, and Cl^- in the PC molecules also increase the passivation ability of NiO_x/perovskite buried defects. This improved passivation helps improve the overall performance of the device. The chemical interaction between PC in Co-SAM and NiO_x was extensively investigated to explore the defect passivation effect of PC on the NiO_x surface. To gain insights into the nature of these interactions, Gaussian calculations were performed to analyze the electrostatic potential of PC. The calculation reveals that the phosphate group and Cl^- exhibit a negatively charged character, indicated by their blue color, suggesting their ability to donate electrons. On the other hand, the quaternary ammonium ion displays a positive charge, as denoted by its green color (Figure 1c). Fourier transform infrared (FTIR) spectra demonstrate that after mixing PC and NiO_x, C–N has no shift and P=O undergoes a red shift of 3 cm^{-1} compared to pure PC, proving that P=O in PC can be chelated to the NiO_x surface (Figure 1d).[16]

X-ray photoelectron spectroscopy (XPS) reveals that Ni ions on the NiO_x/Me-4PACz surface shift to a lower energy level (Figure S1a, Supporting Information), and O shifts to a higher energy level by 0.55 eV (Figure S1b, Supporting Information) than pure NiO_x, proving that the phosphate group in Me-4PACz interacts with NiO_x. Furthermore, when PC is introduced to the NiO_x/Me-4PACz system (NiO_x/Me-4PACz+PC), additional shifts in the energy levels of Ni and O ions are observed. Ni ions further shift to a lower energy level and O shifts to a higher energy level by 0.09 eV, proving that the phosphate group and Cl^- in PC interact with NiO_x. Additionally, an increase in N content (Figure S1c, Supporting Information) and the new element Cl (Figure S1d, Supporting Information) appear on the surface of NiO_x/Me-4PACz+PC, indicating that Me-4PACz and PC coexist on NiO_x surfaces.

To further confirm the interaction between Cl^- in PC and NiO_x, we measured the XRD of NiO_x, PC, and NiO_x+PC. The XRD pattern of NiO_x exhibits prominent (111) and (200) crystal plane peaks (Figure 1e).[17] The introduction of Cl^- from PC results a blue shift of the (200) XRD peak, indicating lattice expansion.[18] Considering that the ionic radius of Cl^- (1.81 Å) is larger than O^{2-} (1.40 Å), the incorporation of Cl^- leads to the expansion of the NiO_x lattice structure. These results prove that PC-terminal phosphate groups can be chelated to the NiO_x surface in a vertically arranged manner. In addition, Cl^- can also be doped into NiO_x to suppress Ni ion defects.

We considered the impact of Co-SAM on the surface roughness and electrical properties of NiO_x. Atomic force microscopy (AFM) can conclude that the surface roughness of Me-4PACz+PC-modified NiO_x (3.56 nm) is smaller than that of Me-4PACz (3.70 nm), with a smoother height change profile (Figure S2, Supporting Information), indicating that Co-SAM makes the NiO_x surface flatter and helps reduce surface defects. Kelvin probe force microscopy (KPFM) was employed to evaluate the average surface contact potential difference (CPD) between NiO_x/Me-4PACz and NiO_x/Me-4PACz+PC films. As shown in Figure 1f–h, the CPD value of NiO_x/Me-4PACz+PC film is lower than that of NiO_x/Me-4PACz film. The reduction of CPD is beneficial to the downward shift of the Fermi level (E_F) of Me-4PACz film, and this result is also proved by Ultraviolet photoelectron spectroscopy (UPS).[19] UPS was employed to measure the valence band (VB) and E_F of HTL (Figures S3–S5, Supporting Information). The VB and E_F values of the Me-4PACz film are −5.34 and −4.44 eV, respectively, while the VB and E_F of the Me-4PACz+PC film decrease to lower levels (VB = −5.43 eV, E_F = −4.58 eV). The lower VB and E_F are beneficial to reducing hole transfer barriers and decreasing nonradiative recombination losses.[20] We further confirmed the densification of SAM or Co-SAM on NiO_x using cyclic voltammetry (CV) measurements. The areal density of Co-SAM on NiO_x is 6.59×10^{13} molecules cm^{-2}, an increase from 6.06×10^{13} molecules cm^{-2} in single SAM (Figure S6 and Note S1, Supporting Information).[21,22] We conclude that Co-SAM is beneficial to forming a uniform and dense coating on the NiO_x surface and optimizing the energy band structure of the SAM layer to enhance hole transport.

We conducted FTIR, XPS, and XRD to elucidate the interaction mechanism between PC in Co-SAM and the bottom surface of the perovskite film. The FTIR spectra show that after mixing PC and PbI_2, P=O and C–N exhibit a red shift of 5 cm^{-1} and 3 cm^{-1}, respectively, compared to pure PC, proving that P=O and C–N in PC can interact with Pb ions on the buried bottom surface of perovskite (**Figure** 2a). XPS shows that, relative to PbI_2, the Pb and I elements experience a downward energy shift after mixing PC and PbI_2 (Figure 2b and Figure S7a, Supporting Information). Simultaneously, the Cl, O, and N elements exhibit an upward energy shift when PC is mixed with PbI_2 compared with PC (Figure S7b–d, Supporting Information), proving that the phosphate groups, quaternary ammonium ions, and Cl^- in PC can engage in Lewis acid–base interactions with Pb. XRD results indicate that mixing PC with PbI_2 completely produces a distinct phase different from PbI_2 and PC, which is a low-dimensional complex $PCPbI_2$ (Figure 2c). Considering the chelation of phosphoric acid in PC to the NiO_x surface, the remaining quaternary ammonium ion and Cl^- interact with the uncoordinated Pb defects on the bottom surface of the perovskite. Specifically, the quaternary ammonium ions, like tetra-methyl ammonium ions,[23] can occupy the FA/MA (methylamine) vacancies within the perovskite lattice and Cl^- may fill the vacancies of anions on the perovskite surface.[24,25]

We utilized Co-SAM to modify NiO_x and investigated its effect on perovskite crystallization through scanning electron microscopy (SEM). Initially, we use ultraviolet (UV) glue to uncover the bottom surface of the perovskite and observe the morphology (Figure 2d,e, Supporting Information). The bottom surface of NiO_x/Me-4PACz has many small pore defects at the grain boundary, and there are almost no small particles of NiO_x, indicating that there is almost no interaction between Me-4PACz and the bottom surface of perovskite, while the grain boundary area on the bottom surface of NiO_x/Me-4PACz+PC is denser and has many small NiO_x particles attached. The introduction of PC molecule exhibits a bridging effect, enhancing the adhesion between NiO_x and the perovskite film. Notably, the bottom surface grains of NiO_x/Me-4PACz+PC has obviously increased from 428 nm (NiO_x/Me-4PACz) to 507 nm (Figure S8a,b, Supporting Information). Next, we observed the morphology of the upper surface of the perovskite film. The mean grain size on the surface of the perovskite film grown on NiO_x/Me-4PACz+PC reaches 400 nm, while the mean grain size on the surface of

© 2024 The Author(s). Advanced Materials published by Wiley-VCH GmbH

15214095, 2024, 16, Downloaded from https://onlinelibrary.wiley.com/doi/10.1002/adma.202311970 by Hong Kong Poly University, Wiley Online Library on [23/06/2024]. See the Terms and Conditions (https://onlinelibrary.wiley.com/terms-and-conditions) on Wiley Online Library for rules of use; OA articles are governed by the applicable Creative Commons License

15214095, 2024, 16, Downloaded from https://onlinelibrary.wiley.com/doi/10.1002/adma.202311970 by Hong Kong Poly University, Wiley Online Library on [23/06/2024]. See the Terms and Conditions (https://onlinelibrary.wiley.com/terms-and-conditions) on Wiley Online Library for rules of use; OA articles are governed by the applicable Creative Commons License

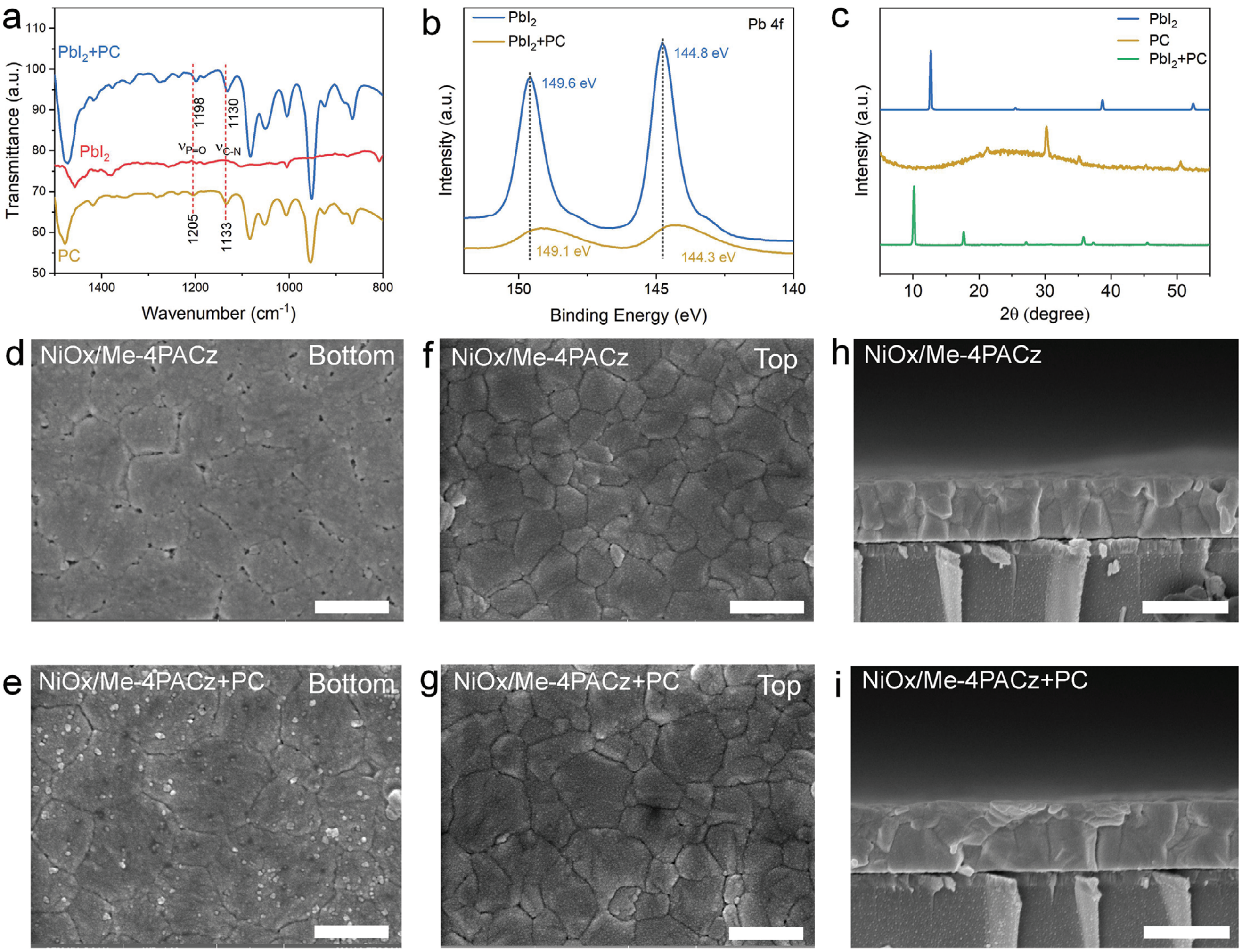

Figure 2. Effect of Co-SAM on crystallization of perovskite films. a) FTIR of PC+PbI_2, PbI_2, and PC. b) XPS of Pb 4f for PC+PbI_2 and PbI_2. c) XRD of PbI_2, PC, and PC+PbI_2. d,e) Bottom, f,g) surface (the scale bar is 500 nm), and h,i) cross-sectional views (the scale bar is 1000 nm) of perovskite films deposited on different transport layers.

the perovskite film grown on NiO_x/Me-4PACz is only 308 nm (Figure 2f,g and Figure S8c,d, Supporting Information), indicating that the presence of Co-SAM facilitates promote grain growth and reduce defects in the perovskite film. The cross-sectional SEM images also present that the grains are vertically arranged, which is beneficial to promoting carrier transport (Figure 2h,i). We conducted further investigation on the changes in crystal quality using XRD. Perovskite films with different transport layers exhibit similar diffraction patterns, which consistent with the characteristic black α-$FAPbI_3$ phase (Figure S9a, Supporting Information).[26] The half-peak width of the (001) peak of the perovskite film on NiO_x/Me-4PACz+PC is found to be narrower (Figure S9b, Supporting Information), indicating an increase in the perovskite grain size, which aligns with the results obtained from SEM. Moreover, the enhanced absorption in the 500–800 nm band further supports the notion of improved crystal quality (Figure S10, Supporting Information). These findings provide evidence that Co-SAM molecules can regulate crystallization and promote the increase in grain size.

As the substrate for perovskite deposition, the surface properties of the HTL profoundly affected the nucleation and crystallization mechanisms of perovskite film. To characterize the wetting behavior of the perovskite precursor solution on the different HTL surface, the contact angle was determined. The contact angle of the perovskite precursor solution on NiO_x/Me-4PACz+PC HTL is determined to be 37.29°, while on NiO_x/Me-4PACz HTL, the contact angle is found to be 34.92°, indicating that the quaternary ammonium groups on PC induce a more hydrophobic surface for precursor solvents (Figure S11, Supporting Information). To investigate the perovskite film formation process on different HTL surfaces, in situ UV–visible (UV–Vis) spectroscopy was performed during spin-coating (**Figure** 3a,b). Initially, the perovskite precursor solution is in a dissolved state before 38 s, with negligible nucleation occurring. Upon the dropwise addition of the antisolvent at 38 s, the absorption intensity across the entire wavelength range starts to increase, indicating the formation of perovskite crystallites. We used the first derivative to calculate the nucleation rate based on the relationship between 600 nm and spin-coating time (Figure 3c).[27] The nucleation rate

© 2024 The Author(s). Advanced Materials published by Wiley-VCH GmbH

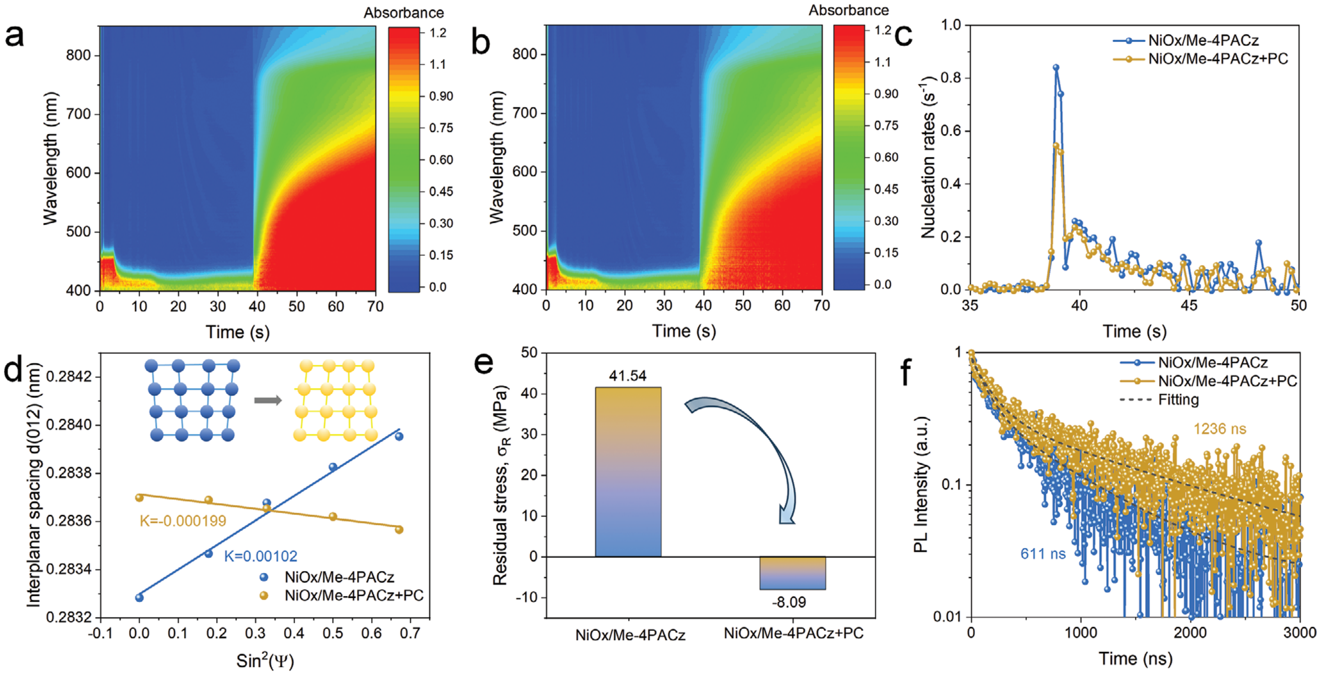

Figure 3. Co-SAM-regulated crystallization kinetics, strain, and carrier recombination. a) In situ UV–Vis of perovskite films deposited on a) NiO_x/Me-4PACz and b) NiO_x/Me-4PACz+PC. c) Calculation of nucleation rates using first derivatives corresponds to in situ UV–Vis spectra. d) D-spacing values obtained from (012) plane as a function of incidence angle (interior illustration: schematic of the transformation from tensile stress to compressive stress). e) Comparison of residual stress for perovskite film deposited on NiO_x/Me-4PACz and NiO_x/Me-4PACz+PC. f) TRPL spectra of perovskite films deposited on NiO_x/Me-4PACz and NiO_x/Me-4PACz+PC.

of NiO_x/Me-4PACz+PC is lower because the nonwetting surface inhibits heterogeneous nucleation, resulting in a reduction in nucleation density and thus a larger grain size.[28] In addition, the strong chemical interaction between PC and PbI_2 in the perovskite leads to a delay in perovskite nucleation, which is also beneficial to obtain highly crystalline perovskite films with large grain sizes.[29]

During the crystallization process of perovskite films (i.e., nucleation and crystal growth), residual tensile stress (σ, note 2) was a common occurrence and a significant contributor to the intrinsic instability of PSCs.[30,31] To investigate the release of residual stress in the perovskite film, grazing incidence X-ray diffraction (GIXRD) measurements were implemented at different tilt angles ($\Psi = 0°, 25°, 35°, 45°, 55°$) (Figure S12, Supporting Information).[32] Through analysis of the GIXRD images acquired at different depths, we obtained the relationship between the interplanar distance (d_n) and $\mathrm{Sin}^2\Psi$. The slope of the d_n-$\mathrm{Sin}^2\Psi$ fitting curve served as an estimation of the residual stress release in the perovskite film (Figure 3d). Perovskite films deposited on single SAM exhibit positive slopes, indicating the presence of tensile stress within the films. Conversely, the slope of the film deposited on Co-SAM becomes slightly negative, confirming the presence of internal compressive stress.[33] Consequently, the tensile stress of the perovskite film deposited on single SAM and the compressive stress of the film deposited on Co-SAM are calculated to be 41.54 and −8.09 MPa, respectively (Figure 3e).[34] When the organic cation vacancies on the buried bottom surface of the perovskite are occupied by the terminal quaternary ammonium ions of PC, the lattice undergoes expansion due to the larger radius of the quaternary ammonium ion (3.20 Å) compared to that of the FA^+ (2.53 Å) and MA^+ (2.17 Å).[35,36] Moreover, Co-SAM adjusts the crystal orientation and reduces bulk defects of perovskite. These effects may cause the perovskite film to change from tensile stress to compressive stress, improving the stability of the perovskite film.[37]

We analyzed the influence of Co-SAM on perovskite carrier transport dynamics using photoluminescence (PL) on glass substrates. Through PL and time-resolved PL (TRPL) spectroscopy, we observe that the PL intensity at the interface between the NiO_x/perovskite film, treated with Co-SAM, is significantly enhanced (Figure S13, Supporting Information). Additionally, the lifetime is increased by ≈50.5%, from 611 to 1236 ns (Figure 3f). These findings indicate that the presence of Co-SAM effectively suppresses interfacial nonradiative recombination processes.

We constructed a typical inverted NiO_x-based PSC device and investigated the impact of Co-SAM on its photovoltaic performance. In our study, we found that PC enhances the defect passivation ability of Me-4PACz at the NiO_x/perovskite film interface, as depicted in **Figure 4**a. The performance of devices modified with different concentrations of Me-4PACz or PC is shown in Figures S14–S16 (Supporting Information). Both 0.5 mg mL^{-1} Me-4PACz or 0.1 mg mL^{-1} PC modified NiO_x can have beneficial effects, but the combination of Me-4PACz and PC demonstrates superior performance. We further investigate the photovoltaic parameters and curves of devices modified with different concentrations of PC doped with Me-4PACz, as shown in Figure 4b. The optimal doping concentration is determined to be 0.1 mg mL^{-1}.

© 2024 The Author(s). Advanced Materials published by Wiley-VCH GmbH

15214095, 2024, 16, Downloaded from https://onlinelibrary.wiley.com/doi/10.1002/adma.202311970 by Hong Kong Poly University, Wiley Online Library on [23/06/2024]. See the Terms and Conditions (https://onlinelibrary.wiley.com/terms-and-conditions) on Wiley Online Library for rules of use; OA articles are governed by the applicable Creative Commons License

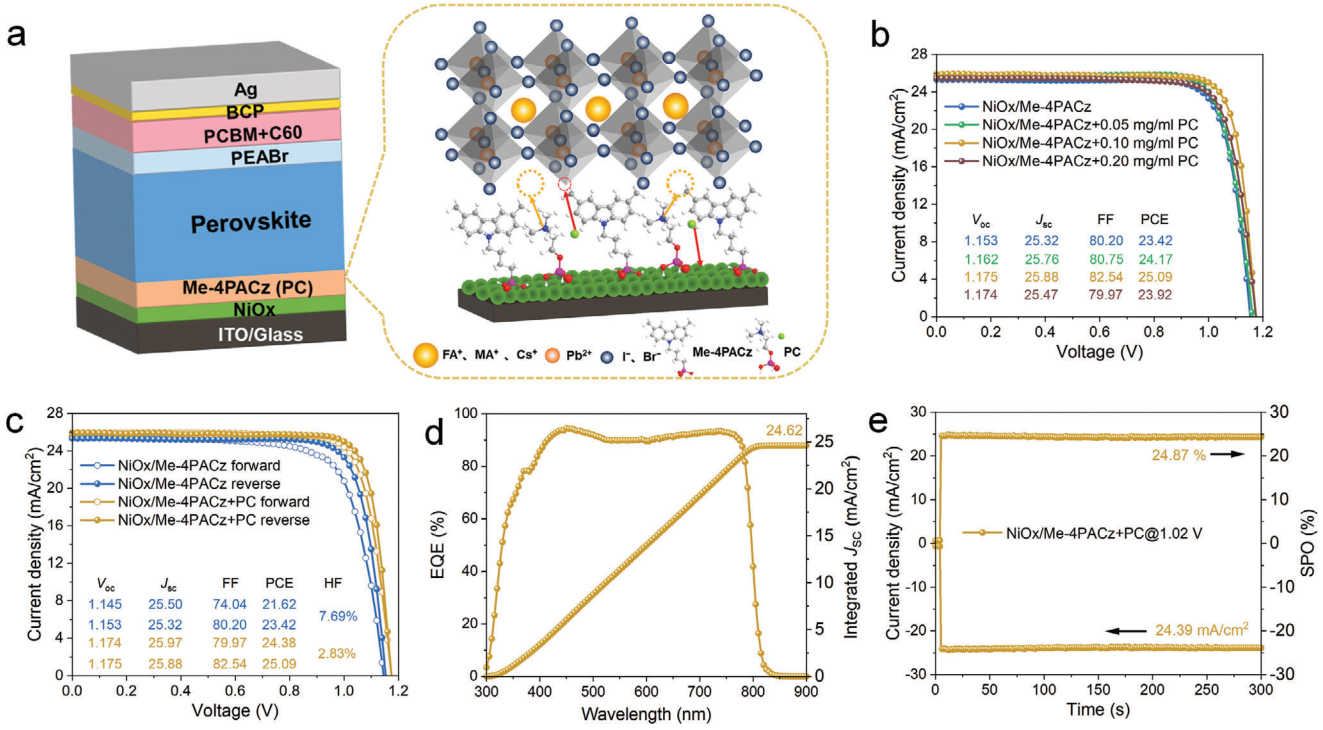

Figure 4. Impact of Co-SAM on device PCE. a) Schematic diagram of the inverted device structure and the interaction role of Co-SAM with NiO$_x$ and perovskite films. b) Effect of Me-4PACz doped with different concentrations of PC on device performance. c) The forward and reverse scanning performance of NiO$_x$-deposited Me-4PACz and Me-4PACz+PC devices. d) EQE and e) steady-state output performance of NiO$_x$/Me-4PACz+PC devices.

Subsequently, the highest PCE of the control and Me-4PACz + 0.1 mg mL^{-1} PC modified device is measured during forward and reverse scans. In reverse scan, the Co-SAM-treated device exhibits an increase in PCE from 23.42% to 25.09%, an increase in V_{OC} from 1.153 to 1.175 V, an increase in short-circuit current density (J_{SC}) from 25.32 to 25.88 mA cm^{-2}, and an increase in fill factor (FF) from 80.20% to 82.54%. In forward scan, the PCE of the Co-SAM-treated device increases from 21.62% to 24.38% (Figure 4c). The hysteresis factor (HF, Note S3, Supporting Information) of Co-SAM-treated is reduced, mainly due to the passivation inhibition and promotion of carrier transport played by PC at the interface.[38] The Co-SAM-treated device achieves an integrated current of 24.62 mA cm^{-2} through external quantum efficiency (EQE) spectra (Figure 4d) and a steady-state output (SPO) efficiency of 24.87% (Figure 4e), both of which are close to the results obtained by the J–V curve. Figure S17 (Supporting Information) shows the photovoltaic parameter statistics chart. The average PCE of the device treated with Co-SAM increases from 22.50 ± 0.41% to 24.38 ± 0.36%, with a reduced standard deviation, demonstrating improved repeatability. To verify the universality of the Co-SAM strategy, we employ O-phospho-DL-serine- and creatinol phosphate-doped Me-4PACz, as well as PC-doped 2PACz-treated devices, which result in efficiencies of 24.55%, 24.38%, and 24.54%, respectively (Figures S18–S20, Supporting Information), proving that simple molecular doping can improve the performance of SAM.

We used the Mott–Schottky method to validate the enhancement of the V_{OC}. The Co-SAM-treated device exhibits a built-in electric field of 1.16 V, surpassing the value of 1.11 V observed in the single SAM-treated device. This enhancement in the electric field is advantageous for facilitating charge transport and improving the V_{OC} in photovoltaic devices (**Figure 5a**).[39] The EQE$_{EL}$ values of 1.90% and 4.35% for the SAM and the Co-SAM-treated device, respectively, can be obtained from the electroluminescence (EL) spectra (Figure 5b). The relatively high EQE$_{EL}$ value indicates that Co-SAM, as an interfacial modifier, can suppress V_{OC} loss caused by nonradiative recombination.[40] In addition, the V_{OC} improvement amount (ΔV_{OC}, Note S4, Supporting Information) after Co-SAM treatment is estimated to be 0.021 V, which is almost consistent with the V_{OC} difference (0.022 V) obtained by J–V.[41]

Co-SAM treatment improves the crystal quality of the perovskite film and helps improve the J_{SC} of the device. To investigate the device's response, we conducted experiments to analyze the relationship between the V_{OC} and the applied light intensity (Figure 5c and Note S5, Supporting Information). The control device shows an ideality factor (n) of 1.52, whereas the Co-SAM-treated device demonstrates a significantly lower n value of 1.12. It is known that the n reflects defect-assisted recombination in devices, and this result further confirms that interfacial recombination in Co-SAM-treated devices has been substantially suppressed, helping to improve the FF of the device.[42]

To explore the amount of defect and hole mobility in the device, space charge limited current (SCLC) was performed.[43] As depicted in Figure 5d, the intersection of the ohmic region and the trap-filling region represents the trap filling limit voltage (V_{TFL}), which is determined to be 1.25 V and 0.87 V for Me-4PACz and Co-SAM treated devices, respectively, with corresponding defect

© 2024 The Author(s). Advanced Materials published by Wiley-VCH GmbH

15214095, 2024, 16, Downloaded from https://onlinelibrary.wiley.com/doi/10.1002/adma.202311970 by Hong Kong Poly University, Wiley Online Library on [23/06/2024]. See the Terms and Conditions (https://onlinelibrary.wiley.com/terms-and-conditions) on Wiley Online Library for rules of use; OA articles are governed by the applicable Creative Commons License

15214095, 2024, 16, Downloaded from https://onlinelibrary.wiley.com/doi/10.1002/adma.202311970 by Hong Kong Poly University, Wiley Online Library on [23/06/2024]. See the Terms and Conditions (https://onlinelibrary.wiley.com/terms-and-conditions) on Wiley Online Library for rules of use; OA articles are governed by the applicable Creative Commons License

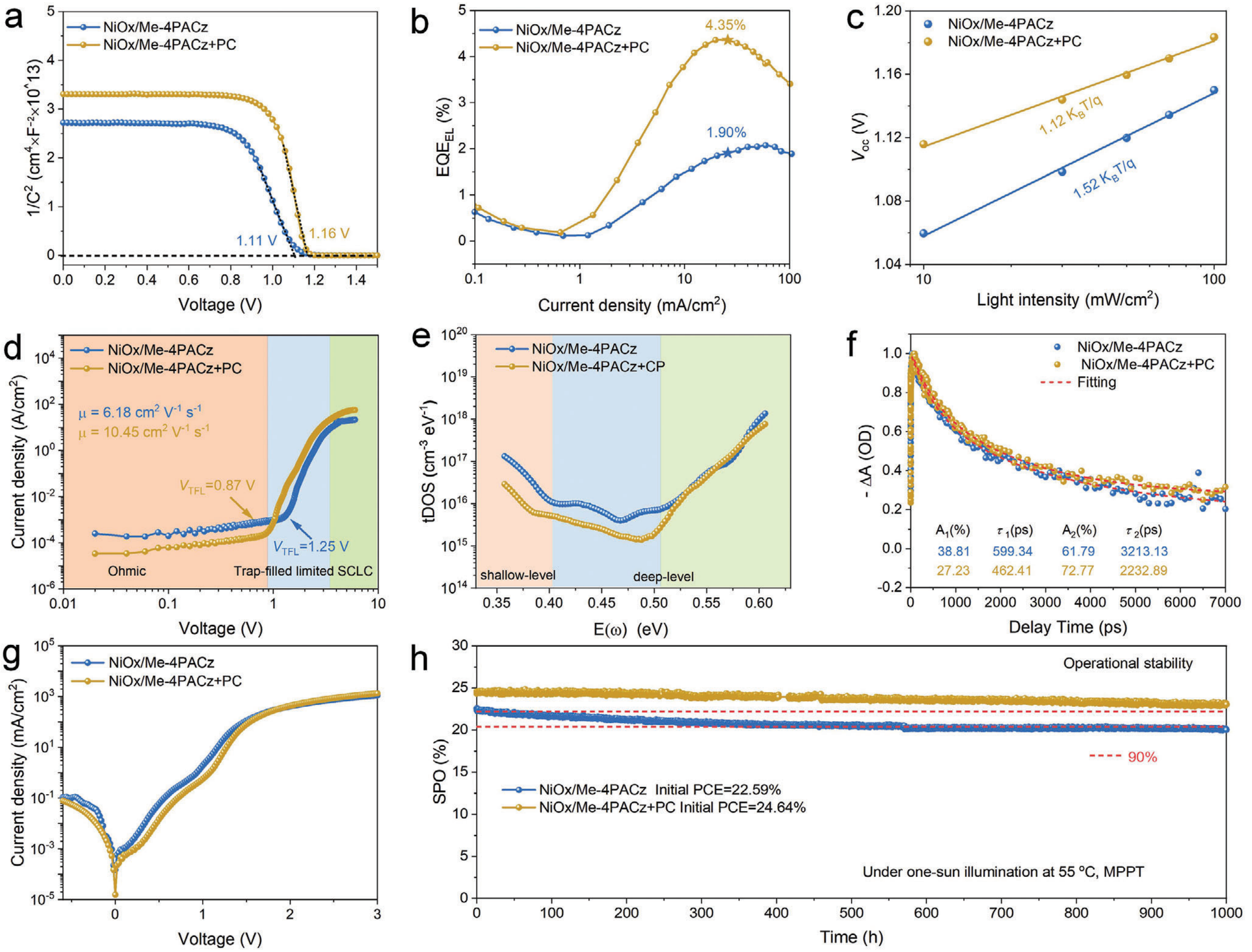

Figure 5. Carrier dynamics and stability. a) Mott–Schottky analysis. b) EQE_{EL} values of the PSCs. c) Light intensity dependence of V_{OC} of PSCs. d) SCLC of the hole-only devices. e) tDOS curves of PSC devices employing NiO_x/Me-4PACz and NiO_x/Me-4PACz+PC. f) Decay of the bleaching signal of perovskite films. g) Dark *J–V* curves of PSCs with different substrates. h) SPO of the encapsulated PSCs measured at MPP under continuous one-sun illumination.

state densities of 5.52×10^{15} cm^{-3} and 3.84×10^{15} cm^{-3} (Note S6, Supporting Information).[44] Depending on the SCLC region, the hole mobility is 6.18 and 10.45 cm^2 V^{-1} s^{-1} for Me-4PACz and Co-SAM treated devices (Note S6, Supporting Information). These results prove that Co-SAM can suppress device defects and accelerate hole transport.[45] Furthermore, to determine the type of device defect, we conducted an admittance spectrum test (Figure 5e and Note S7, Supporting Information). Compared with single SAM, Co-SAM-treated devices reduce both deep and shallow energy level defects (surface and grain boundary defects), which shows that Co-SAM regulates perovskite crystallization, promotes better crystallinity of perovskite, and reduces the grain boundaries and surface defects of the perovskite film.[46]

Femtosecond transient absorption spectroscopy was further used to analyze the carrier dynamics in perovskite films deposited on single SAM and Co-SAM (Figure S21, Supporting Information). It can be seen that the ground-state bleaching decay rate of the perovskite film deposited on Co-SAM is significantly enhanced,[47] and the lifetime of the double-exponential kinetic model is simultaneously reduced, which once again verifies that Co-SAM can promote carrier transport (Figure 5f).[34] Additionally, the better coverage of Co-SAM on the substrate effectively reduces the leakage current, further demonstrating the beneficial effect of Co-SAM in optimizing device performance (Figure 5g).[48]

The operational stability of the encapsulated devices was evaluated under maximum power point (MPP) tracking and exposure to a white light-emitting diode (LED) lamp with the same intensity as one-sunlight (without UV filter) in ambient air at a temperature of 55 °C. In Figure 5h, it can be observed that the control device, with an initial efficiency of ≈22.59%, exhibits relatively rapid degradation, retaining only about 88% of its initial PCE after 1000 h. According to the principle of linear attenuation, the single SAM-treated device retains 80% of its initial value for an extended duration of ≈2455 h. In contrast, the device treated with a Co-SAM treatment shows slower decay in performance after 1000 h of continuous running. It retains about 93% of its initial PCE (24.64%). The estimated T_{80} time for the

© 2024 The Author(s). Advanced Materials published by Wiley-VCH GmbH

Co-SAM-treated device is ≈3139 h. The Co-SAM treatment significantly improves the operational stability of the encapsulated PSCs, mainly by suppressing device defects and stabilizing the perovskite crystals.[49,50]

3. Conclusion

In summary, we use PC together with Me-4PACz to form Co-SAM on NiO_x surface to optimize the buried interface in PSC. The phosphate group and Cl^- in PC can inhibit NiO_x surface defects. Meantime, the quaternary ammonium ions and Cl^- in PC can fill organic cations and halogen vacancies defects at the bottom of the perovskite film. Co-SAM can promote the growth of perovskite crystals, passivate buried defects, suppress nonradiative recombination, optimize the energy band alignment to facilitate carrier transmission, and relieve the residual stress of the perovskite film. As a result, the average device PCE is substantially enhanced from 22.50 ± 0.41% to 24.38 ± 0.36% with a champion efficiency of 25.09%. Moreover, the device can retain 93% of the initial value after continuous running for 1000 h under one-sun illumination. This work demonstrates the advantages of modifying Co-SAM on NiO_x HTL in PSCs.

Supporting Information

Supporting Information is available from the Wiley Online Library or from the author.

Acknowledgements

This research was supported by the National Natural Science Foundation of China (22305191), Postdoctoral Research Project Funding in Shaanxi Province, the Hong Kong Scholars Program (XJ2022025), the Research Grants Council (RGC) of Hong Kong, China (Project No. 15306822), and the Hong Kong Polytechnic University, Hong Kong, China (ZE2X).

Conflict of Interest

The authors declare no conflict of interest.

Data Availability Statement

The data that support the findings of this study are available from the corresponding author upon reasonable request.

Keywords

buried interface, inverted perovskite solar cells, self-assembled monolayer

Received: November 11, 2023
Revised: December 15, 2023
Published online: January 15, 2024

[1] H. Zhang, C. Zhao, J. Yao, W. C. H. Choy, *Angew. Chem., Int. Ed.* **2023**, *62*, 202219307.
[2] Z. Li, X. Sun, X. Zheng, B. Li, D. Gao, S. Zhang, X. Wu, S. Li, J. Gong, J. M. Luther, Z. Li, Z. Zhu, *Science* **2023**, *382*, 284.
[3] F. Ma, Y. Zhao, J. Li, X. Zhang, H. Gu, J. You, *J. Energy Chem.* **2021**, *52*, 393.
[4] Z.-W. Gao, Y. Wang, W. C. H. Choy, *Adv. Energy Mater.* **2022**, *12*, 2104030.
[5] C. C. Boyd, R. C. Shallcross, T. Moot, R. Kerner, L. Bertoluzzi, A. Onno, S. Kavadiya, C. Chosy, E. J. Wolf, J. Werner, J. A. Raiford, C. De Paula, A. F. Palmstrom, Z. J. Yu, J. J. Berry, S. F. Bent, Z. C. Holman, J. M. Luther, E. L. Ratcliff, N. R. Armstrong, M. D. Mcgehee, *Joule* **2020**, *4*, 1759.
[6] W. Chen, Y. Zhou, G. Chen, Y. Wu, B. Tu, F.-Z. Liu, L. Huang, A. M. C. Ng, A. B. Djurisic, Z. He, *Adv. Energy Mater.* **2019**, *9*, 1803872.
[7] X. Zhu, C. F. J. Lau, K. Mo, S. Cheng, Y. Xu, R. Li, C. Wang, Q. Zheng, Y. Liu, T. Wang, Q. Lin, Z. Wang, *Nano Energy* **2022**, *103*, 107849.
[8] C. Li, X. Wang, E. Bi, F. Jiang, S. M. Park, Y. Li, L. Chen, Z. Wang, L. Zeng, H. Chen, Y. Liu, C. R. Grice, A. Abudulimu, J. Chung, Y. Xian, T. Zhu, H. Lai, B. Chen, R. J. Ellingson, F. Fu, D. S. Ginger, Z. Song, E. H. Sargent, Y. Yan, *Science* **2023**, *379*, 690.
[9] T. Wang, F. Zheng, G. Tang, J. Cao, P. You, J. Zhao, F. Yan, *Adv. Sci.* **2021**, *8*, 2004315.
[10] L. Li, Y. Wang, X. Wang, R. Lin, X. Luo, Z. Liu, K. Zhou, S. Xiong, Q. Bao, G. Chen, Y. Tian, Y. Deng, K. Xiao, J. Wu, M. I. Saidaminov, H. Lin, C.-Q. Ma, Z. Zhao, Y. Wu, L. Zhang, H. Tan, *Nat. Energy* **2022**, *7*, 708.
[11] Y. Huang, B. Wang, T. Liu, D. Li, Y. Zhang, T. Zhang, X. Yao, Y. Wang, A. Amini, Y. Cai, B. Xu, Z. Tang, G. Xing, C. Cheng, *Adv. Funct. Mater.* **2023**, *33*, 2302375.
[12] R. He, W. Wang, Z. Yi, F. Lang, C. Chen, J. Luo, J. Zhu, J. Thiesbrummel, S. Shah, K. Wei, Y. Luo, C. Wang, H. Lai, H. Huang, J. Zhou, B. Zou, X. Yin, S. Ren, X. Hao, L. Wu, J. Zhang, J. Zhang, M. Stolterfoht, F. Fu, W. Tang, D. Zhao, *Nature* **2023**, *618*, 80.
[13] S. Zhang, F. Ye, X. Wang, R. Chen, H. Zhang, L. Zhan, X. Jiang, Y. Li, X. Ji, S. Liu, M. Yu, F. Yu, Y. Zhang, R. Wu, Z. Liu, Z. Ning, D. Neher, L. Han, Y. Lin, H. Tian, W. Chen, M. Stolterfoht, L. Zhang, W.-H. Zhu, Y. Wu, *Science* **2023**, *380*, 404.
[14] L. Mao, T. Yang, H. Zhang, J. Shi, Y. Hu, P. Zeng, F. Li, J. Gong, X. Fang, Y. Sun, X. Liu, J. Du, A. Han, L. Zhang, W. Liu, F. Meng, X. Cui, Z. Liu, M. Liu, *Adv. Mater.* **2022**, *34*, 2206193.
[15] Q. Jiang, R. Tirawat, R. A. Kerner, E. A. Gaulding, Y. Xian, X. Wang, J. M. Newkirk, Y. Yan, J. J. Berry, K. Zhu, *Nature* **2023**, *623*, 313.
[16] B. Niu, H. Liu, Y. Huang, E. Gu, M. Yan, Z. Shen, K. Yan, B. Yan, J. Yao, Y. Fang, H. Chen, C.-Z. Li, *Adv. Mater.* **2023**, *35*, 2212258.
[17] I. Kafedjiska, I. Levine, A. Musiienko, N. Maticiuc, T. Bertram, A. Al-Ashouri, C. A. Kaufmann, S. Albrecht, R. Schlatmann, I. Lauermann, *Adv. Funct. Mater.* **2023**, *33*, 2302924.
[18] J. Tao, X. Liu, J. Shen, S. Han, L. Guan, G. Fu, D.-B. Kuang, S. Yang, *ACS Nano* **2022**, *16*, 10798.
[19] L. Yang, H. Zhou, Y. Duan, M. Wu, K. He, Y. Li, D. Xu, H. Zou, S. Yang, Z. Fang, S. Liu, Z. Liu, *Adv. Mater.* **2023**, *35*, 2211545.
[20] D. Zhang, X. Wang, T. Tian, X. Xia, J. Duan, Z. Fan, F. Li, *Chem. Eng. J.* **2023**, *469*, 143789.
[21] M. Liu, L. Bi, W. Jiang, Z. Zeng, S.-W. Tsang, F. R. Lin, A. K.-Y. Jen, *Adv. Mater.* **2023**, 2304415.
[22] S. M. Park, M. Wei, N. Lempesis, W. Yu, T. Hossain, L. Agosta, V. Carnevali, H. R. Atapattu, P. Serles, F. T. Eickemeyer, H. Shin, M. Vafaie, D. Choi, K. Darabi, E. D. Jung, Y. Yang, D. B. Kim, S. M. Zakeeruddin, B. Chen, A. Amassian, T. Filleter, M. G. Kanatzidis, K. R. Graham, L. Xiao, U. Rothlisberger, M. Grätzel, E. H. Sargent, *Nature* **2023**, *624*, 289.
[23] S. Yang, Y. Wang, P. Liu, Y.-B. Cheng, H. J. Zhao, H. G. Yang, *Nat. Energy* **2016**, *1*, 15016.
[24] Q. Zhou, J. Qiu, R. Zhuang, M. Yu, J. Liu, Y. Hua, L. Ding, X. Zhang, *ACS Appl. Mater. Interfaces* **2023**, *15*, 40676.

© 2024 The Author(s). Advanced Materials published by Wiley-VCH GmbH

15214095, 2024, 16, Downloaded from https://onlinelibrary.wiley.com/doi/10.1002/adma.202311970 by Hong Kong Poly University, Wiley Online Library on [23/06/2024]. See the Terms and Conditions (https://onlinelibrary.wiley.com/terms-and-conditions) on Wiley Online Library for rules of use; OA articles are governed by the applicable Creative Commons License

[25] C. Liu, L. Huang, X. Zhou, X. Wang, J. Yao, Z. Liu, S. F. Liu, W. Ma, B. Xu, *Sci. Bull.* **2021**, *66*, 1419.

[26] Q. Cao, Y. Li, Y. Zhang, J. Zhao, T. Wang, B. Yang, X. Pu, J. Yang, H. Chen, X. Chen, X. Li, S. Ghasemi, H. Salari, A. Hagfeldt, X. Li, *Adv. Energy Mater.* **2022**, *12*, 2201435.

[27] Q. Liang, K. Liu, M. Sun, Z. Ren, P. W. K. Fong, J. Huang, M. Qin, Z. Wu, D. Shen, C.-S. Lee, J. Hao, X. Lu, B. Huang, G. Li, *Adv. Mater.* **2022**, *34*, 2200276.

[28] C. Bi, Q. Wang, Y. Shao, Y. Yuan, Z. Xiao, J. Huang, *Nat. Commun.* **2015**, *6*, 7747.

[29] N. Wu, T. Yang, Z. Wang, Y. Wu, Y. Wang, C. Ma, H. Li, Y. Du, D. Zhao, S. Wang, P. Liu, W. Huang, X. Ren, S. F. Liu, K. Zhao, *Adv. Mater.* **2023**, *35*, 2304809.

[30] H. Zhang, N.-G. Park, *Angew. Chem., Int. Ed.* **2022**, *61*, 202212268.

[31] B. Yang, D. Bogachuk, J. Suo, L. Wagner, H. Kim, J. Lim, A. Hinsch, G. Boschloo, M. K. Nazeeruddin, A. Hagfeldt, *Chem. Soc. Rev.* **2022**, *51*, 7509.

[32] N. Rolston, K. A. Bush, A. D. Printz, A. Gold-Parker, Y. Ding, M. F. Toney, M. D. Mcgehee, R. H. Dauskardt, *Adv. Energy Mater.* **2018**, *8*, 1802139.

[33] H. Zhang, Z. Chen, M. Qin, Z. Ren, K. Liu, J. Huang, D. Shen, Z. Wu, Y. Zhang, J. Hao, C.-S. Lee, X. Lu, Z. Zheng, W. Yu, G. Li, *Adv. Mater.* **2021**, *33*, 2008487.

[34] X. Chang, J.-X. Zhong, S. Li, Q. Yao, Y. Fang, G. Yang, Y. Tan, Q. Xue, L. Qiu, Q. Wang, Y. Peng, W.-Q. Wu, *Angew. Chem., Int. Ed.* **2023**, *62*, 202309292.

[35] H. Wei, Y. Yang, S. Chen, H. J. Xiang, *Nat. Commun.* **2021**, *12*, 637.

[36] M. Saliba, T. Matsui, K. Domanski, J.-Y. Seo, A. Ummadisingu, S. M. Zakeeruddin, J.-P. Correa-Baena, W. R. Tress, A. Abate, A. Hagfeldt, M. Grätzel, *Science* **2016**, *354*, 206.

[37] C.-C. Zhang, S. Yuan, Y.-H. Lou, Q.-W. Liu, M. Li, H. Okada, Z.-K. Wang, *Adv. Mater.* **2020**, *32*, 2001479.

[38] J. Yang, T. Wang, Y. Li, X. Pu, H. Chen, Y. Li, B. Yang, Y. Zhang, J. Zhao, Q. Cao, X. Chen, S. Ghasemi, A. Hagfeldt, X. Li, *Sol. RRL* **2022**, *6*, 2200422.

[39] T. Wang, Y. Li, Q. Cao, J. Yang, B. Yang, X. Pu, Y. Zhang, J. Zhao, Y. Zhang, H. Chen, A. Hagfeldt, X. Li, *Energy Environ. Sci.* **2022**, *15*, 4414.

[40] Z. Li, B. Li, X. Wu, S. A. Sheppard, S. Zhang, D. Gao, N. J. Long, Z. Zhu, *Science* **2022**, *376*, 416.

[41] Q. Jiang, Y. Zhao, X. Zhang, X. Yang, Y. Chen, Z. Chu, Q. Ye, X. Li, Z. Yin, J. You, *Nat. Photonics* **2019**, *13*, 460.

[42] Q. Cao, Y. Zhang, X. Pu, J. Zhao, T. Wang, K. Zhang, H. Chen, X. He, J. Yang, C. Zhang, X. Li, *J. Energy Chem.* **2023**, *86*, 9.

[43] H. Cheng, C. Liu, J. Zhuang, J. Cao, T. Wang, W.-Y. Wong, F. Yan, *Adv. Funct. Mater.* **2022**, *32*, 2204880.

[44] H. Chen, J. Yang, Q. Cao, T. Wang, X. Pu, X. He, X. Chen, X. Li, *Nano Energy* **2023**, *117*, 108883.

[45] Q. Cao, J. Yang, T. Wang, Y. Li, X. Pu, J. Zhao, Y. Zhang, H. Zhou, X. Li, X. Li, *Energy Environ. Sci.* **2021**, *14*, 5406.

[46] X. Pu, J. Zhao, Y. Li, Y. Zhang, H.-L. Loi, T. Wang, H. Chen, X. He, J. Yang, X. Ma, X. Li, Q. Cao, *Nano Energy* **2023**, *112*, 108506.

[47] R. Chen, J. Wang, Z. Liu, F. Ren, S. Liu, J. Zhou, H. Wang, X. Meng, Z. Zhang, X. Guan, W. Liang, P. A. Troshin, Y. Qi, L. Han, W. Chen, *Nat. Energy* **2023**, *8*, 839.

[48] X. Deng, F. Qi, F. Li, S. Wu, F. R. Lin, Z. Zhang, Z. Guan, Z. Yang, C.-S. Lee, A. K.-Y. Jen, *Angew. Chem., Int. Ed.* **2022**, *61*, 202203088.

[49] J. Zhuang, J. Wang, F. Yan, *Nano-Micro Lett.* **2023**, *15*, 84.

[50] P. Shi, Y. Ding, B. Ding, Q. Xing, T. Kodalle, C. M. Sutter-Fella, I. Yavuz, C. Yao, W. Fan, J. Xu, Y. Tian, D. Gu, K. Zhao, S. Tan, X. Zhang, L. Yao, P. J. Dyson, J. L. Slack, D. Yang, J. Xue, M. K. Nazeeruddin, Y. Yang, R. Wang, *Nature* **2023**, *620*, 323.

© 2024 The Author(s). Advanced Materials published by Wiley-VCH GmbH

15214095, 2024, 16, Downloaded from https://onlinelibrary.wiley.com/doi/10.1002/adma.202311970 by Hong Kong Poly University, Wiley Online Library on [23/06/2024]. See the Terms and Conditions (https://onlinelibrary.wiley.com/terms-and-conditions) on Wiley Online Library for rules of use; OA articles are governed by the applicable Creative Commons License